# New aerodynamic lens injector for single particle diffractive imaging

Nils Roth,[1,2] Daniel A. Horke,[1,3,4] Jannik Lübke,[1,2,3] Amit K. Samanta,[1,3] Armando D. Estillore,[1] Lena Worbs,[1,2] Nicolai Pohlman,[1] Kartik Ayyer,[1,3,5] Andrew Morgan,[1] Holger Fleckenstein,[1] Martin Domaracky,[1] Benjamin Erk,[6] Christopher Passow,[6] Jonathan Correa,[6] Oleksandr Yefanov,[1] Anton Barty,[1] Saša Bajt,[1,3] Richard A. Kirian,[7] Henry N. Chapman,[1,2,3] and Jochen Küpper[1,2,3,*]

[1] *Center for Free-Electron Laser Science CFEL, Deutsches Elektronen-Synchrotron DESY, Notkestraße 85, 22607 Hamburg, Germany*
[2] *Department of Physics, Universität Hamburg, Luruper Chaussee 149, 22761 Hamburg, Germany*
[3] *Center for Ultrafast Imaging, Universität Hamburg, Luruper Chaussee 149, 22761 Hamburg, Germany*
[4] *Radboud University, Institute for Molecules and Materials, Heyendaalseweg 135, 6525 AJ Nijmegen, The Netherlands*
[5] *Max-Planck-Institut für Struktur und Dynamik der Materie, Luruper Chaussee 149, 22761 Hamburg, Germany*
[6] *Deutsches Elektronen-Synchrotron DESY, Notkestraße 85, 22607 Hamburg, Germany*
[7] *Department of Physics, Arizona State University, PO Box 871004, Tempe AZ 85287-1004*

(Dated: 2023-10-24)

An aerodynamic lens injector was developed specifically for the needs of single-particle diffractive imaging experiments at free-electron lasers. Its design allows for quick changes of injector geometries and focusing properties in order to optimize injection for specific individual samples. Here, we present results of its first use at the FLASH free-electron-laser facility. Recorded diffraction patterns of polystyrene spheres are modeled using Mie scattering, which allowed for the characterization of the particle beam under diffractive-imaging conditions and yielded good agreement with particle-trajectory simulations.
The complex refractive index of polystyrene at $\lambda = 4.5$ nm was determined as $m = 0.976 - 0.001i$.

## I. INTRODUCTION

Single-particle diffractive imaging (SPI) at free-electron lasers (FELs) promises the recording of three dimensional structures of biological macromolecules and nanoparticles with atomic spatial resolution [1, 2]. The use of hard x-rays from FEL sources for imaging intact molecules is enabled by ultrashort pulse durations that outrun radiation damage [3]. The three-dimensional structure can be reconstructed through careful analysis of millions of diffraction patterns from identical particles [2, 4–6]. Since every diffraction event destroys the sample [7] a continuous source of these identical particles is needed. In comparison to serial crystallography, where the diffraction signal is enhanced by the Bragg conditions of the crystalline structure of the sample, SPI of biomolecules in the range of 10–200 nm struggles a lot more with the signal to noise ratio of individual patterns. With SPI it is possible to record structures of samples that cannot be crystallized, but the brilliance of current FELs necessitate a reduced background, the collection of even more diffraction patterns, and a smaller focus of the FEL x-ray beam for higher intensities. While several successful attempts of SPI have been reported [1, 8, 9], including the imaging of time-resolved structural dynamics [10], all of the mentioned additional requirements are up to now a challenge, especially also for sample injection.

Aerosol injectors proved to be a promising technique for delivering nanoparticles at high densities to the x-ray focus while keeping the background signal low, e. g., compared to liquid or fixed target based delivery methods [11, 12]. Commonly used injectors in SPI experiments are aerodynamic lens stacks (ALS), designed to transmit nanoparticles over a wide size range (∼30 nm–1 µm). However, as we pointed out before [13] even higher densities can be achieved by optimizing the geometry of the injector for the individual sample particles. We developed a new ALS system tailored to the needs of SPI experiments, i. e., allowing for fast changes of the geometry in order to enable optimized injection for every sample. This new ALS was demonstrated and characterized during a beam time at the Free-Electron Laser in Hamburg FLASH.

## II. METHODS

### A. Experimental setup at FLASH

While the ALS presented here is used for an SPI experiment for the first time, it is completely compatible with existing injection hardware and aerosolization methods, e. g., used at FEL endstations and in our in-house injector-characterization setup [14]. For the experimental characterization of the new injector at the CAMP endstation[15] at FLASH [16] polystyrene (PS) spheres with diameters of 220 nm and 88 nm, both with a coefficient of variance of 8 % (certificate of analysis by Alfa Aesar), were used. The sample was provided in water with a concentration of $\sim 3 \cdot 10^{11}$ particles/ml for the 220 nm and $\sim 5 \cdot 10^{11}$ particles/ml for the 88 nm spheres. For aerosolization gas-dynamic virtual nozzles (GDVN) [11] with a ceramic micro-injection-molded tip and a borosilicate glass capillary (inner diameter 20 µm) sample line were used with a

* Email: jochen.kuepper@cfel.de; website: https://www.controlled-molecule-imaging.org

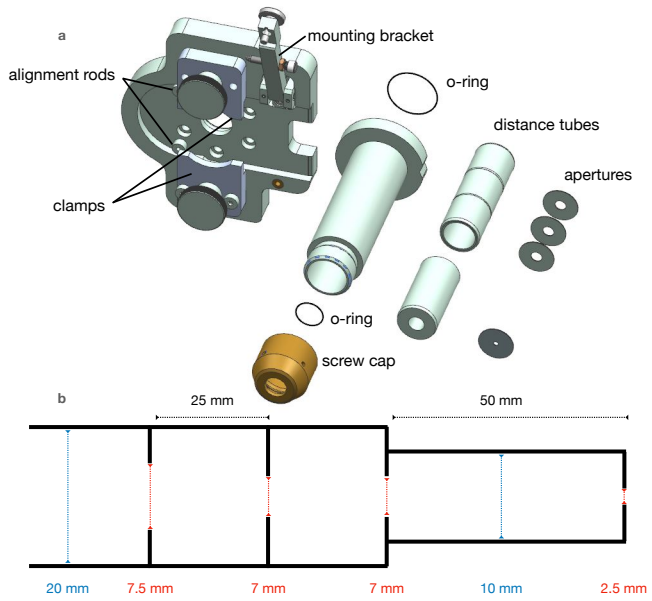


FIG. 1. a) The quick release mount, that attaches the ALS to the aerosol transport tube. The new ALS and its parts. b) The geometry of the ALS set-up used at the experiment at FLASH.

typical sample-solution flowrate of 2 µl/min. FLASH was operated at $\lambda = 4.5$ nm providing pulse trains at 10 Hz with 100 pulses per train, a 1 MHz intra-train repetition rate, and an average pulse energy of ∼15 µJ. The area of the x-ray focus was nominally $6 \times 8$ µm$^2$, but not explicitly measured. For the reduction of background a post-sample aperture [17] was used. The pnCCD detector [18] recorded one integrated frame per pulse train. Frames with blocked x-rays were taken for dark calibration roughly every hour. The distance between the detector plane and the x-ray focus was ∼70 mm.

### B. Aerodynamic lens stack

We implemented the new ALS by attaching it to the aerosolization set-up at the end of the tube that transports the aerosol into the interaction chamber through a quick release mechanism. Fig. 1 a shows the ALS and the quick mount. The ALS can be inserted into the mount from the side. A screw in the mounting bracket, together with two alignment rods, ensures that the round base of the ALS is centered in the correct position. Two clamps press the ALS base and its o-ring against the mount. The ALS shell consists of a tube with a round base for the quick release mount and a screwcap. The total length of the tube with the screwcap is 133.5 mm. The tube has an inner diameter of 25 mm and an outer diameter of 35 mm. Several smaller tubes with matching outer diameter and variable inner diameter can be inserted into the ALS shell. Each of these has a slot for a 0.5 mm thin pinhole aperture. The set of tubes and apertures is fixed in place by the screwcap. Different samples ask for different sets of aerodynamic lenses (ADL) in the ALS stack [13]. By changing the inner diameter of the tubes, their lengths, or the aperture pinhole sizes the ALS can be individualized. This is easily implemented through the replacement of single parts. Having a set of apertures and tubes with different geometries in stock, together with the quick release mount, allows for fast adaption of the ALS without the need for manufacturing or time consuming disassembling of the sample injection set-up. Furthermore, this concept also allows replacing of the tubes and apertures with more complex geometries. Some parts are made of different materials in order to prevent cold welding: The screwcap is made of copper while the tube, the clamps, and the pinhole apertures are made of stainless steel. The mounting plate, the mounting bracket, and the distance tubes are made of aluminum. The o-ring is made of viton.

During the beam time at FLASH the same experimental apparatus was used for other, biological, samples as well. The ALS geometry was not optimized explicitly for the samples used here and the geometry and the injection conditions were kept constant for both PS sizes. The exact geometry is shown in Fig. 1 b. The ALS was mounted onto a motorized $XYZ$ manipulator such that the particle beam could be moved across the x-ray focus. Due to mechanical restrictions in the endstation setup, i. e., the specific post-sample aperture [17] that was kept very close to the interaction region to avoid shadowing of diffraction, the ALS was kept at a rather large distance of ∼16.5 mm from the x-ray focus. This could be avoided by improved post-sample-aperture geometries.

### C. Trajectory simulation

The ALS performance and resulting particle beam profile were simulated using our previously developed simulation framework for ALS injectors [13, 19]. Details of the optimization procedure, including the experimental benchmarking of the optimized geometry for different types of nanoparticles, were reported elsewhere [20]. The flow field of the helium carrier gas through the differential pumping between GDVN and ALS as well as the flow field through the ALS were calculated using the finite-elements method solving the Navier-Stokes equations [21]. Trajectories of individual PS spheres were calculated using Stokes' drag force. While the overall procedure and assumptions were the same as reported previously [13, 20], the boundary conditions and the geometry, see Fig. 1, were adapted to the current experimental conditions. The most significant adjusted simulation parameters are the mass flow of the helium entering the aerosol injector from the GDVN and the measured pressure in the tube directly before the ALS. The former is used as the boundary condition for simulating the differential pumping stage and was set to 100 mg/min. The pressure before the ALS was measured

to be 1.4 mbar.

### D. Pattern classification

Following dark calibration and correction of bad detector pixels, only frames containing at least 500 of the 542394 remaining pixels above the one-photon level were retained for analysis. The known spherical structure of the PS particle was used to differentiate between camera frames that recorded a diffraction pattern of single sample particles and patterns from clusters of sample or any other impurity that might have been recorded. The diffraction pattern of a PS particle was modeled by the calculated Mie scattering of a homogeneous sphere using the `mieptython` library [22]. The complex refractive index for this calculation, the position of the x-ray focus relative to the detector, and the mean particle diameter were obtained by fitting the model to the sum of all 20964 hits collected while injecting 220 nm PS spheres. The fitness function was $F = 1 - P(f, g)$ with the Pearson correlation $P$ of the one dimensional representations of the summed experimental (f) and the modeled (g) pattern. The complex refractive index obtained was assumed to be the same for all PS particles. With this refractive index and the x-ray focus position every single diffraction pattern was modeled individually using the same model; the radii of the particles were again fitted using the same fitness function as above. 6745 diffraction patterns for 220 nm particles and 1893 patterns for 88 nm particles with a similarity of $P(f, g) > 0.3$ were kept for further analysis. Histogramming the diffraction patterns per transverse injector position yielded a two-dimensional projection of the particle beam profile at a distance of 16.5 mm from the injector tip.

## III. RESULTS & DISCUSSION

Fig. 2 shows the sum of the 20964 experimental patterns for 220 nm PS particles in comparison to the fitted model, both as a 2D image and a radial plot. Fig. 2 a shows a section of the left half of the upper detector with the measured data. The corresponding modeled section of the left half of the upper detector is shown in Fig. 2 c mirrored around the $x$ axis. Fig. 2 b, d shows a section of the right half of the upper detector. This time the measured data is mirrored around the $x$ axis and shown in Fig. 2 d. Accordingly, Fig. 2 b is the modeled right detector half. Fig. 2 e is a radial plot comparing the angularly integrated experimental and fitted model data. As described above, this fitted model is used to obtain static parameters such as the distance to the x-ray focus and the refractive index of the PS spheres. Reasonable agreement regarding both the intensities and the fringe spacing was observed, especially for the low diffraction orders. The experimental data is the sum of all diffraction patterns for 220 nm PS particles, i. e., an average of the size distribution of the sample. To this we fit the pattern of a single spherical object corresponding to the mean size of the contributing particles. However, in the experiment the intensity contrast between maxima and minima were smeared out by the size distribution and as this scales with radius this contrast reduction is most pronounced for higher-order peaks. Also noticeable is the slowly falling tail in the experimental radial intensity profile compared to the simulation, which we attribute to the scattering background due to the injection system. The injection system, including the ALS, does have an influence on the quality of the measurable diffraction patterns, e. g., by changing the scattering background caused by the transportation medium or by defining the sample purity. From the fitted model considering both fringe spacing and intensities, we obtained a mean diameter of the PS spheres of 222.5 nm, which nicely agree with the manufacturer specifications. From this fit, we also obtained a refractive index for PS at a wavelength of 4.5 nm of $m = 0.976 - 0.001i$. We point out that our derivation is not very sensitive to the real part of the refractive index. To our knowledge, no comparable values are available; using theoretical predictions for atomic carbon [23] for 4.5 nm and 1050 kg/m$^3$, the density of PS, the refractive index would be approximately $m_C \approx 0.999 - 0.0001i$, which is in fair agreement with our experimental value.

Fitting the 6745 and 1893 individual diffraction patterns of 220 nm and 88 nm PS particles result in mean particle sizes of $223 \pm 7$ nm and $93 \pm 5$ nm, respectively. Comparing this with the specifications given by the manufacturer ($220 \pm 18$ nm and $88 \pm 7$ nm) further increases the confidence in our analysis. For the larger PS spheres the obtained mean diameter is within 2 % and for the smaller within 6 % variation from the specified size, well within the manufacturer's 8 % confidence range.

Fig. 3 shows the simulated beam width containing 90 %

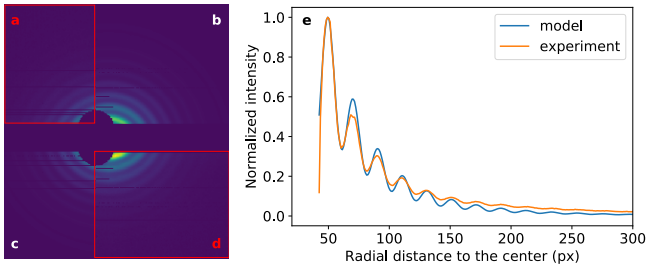


FIG. 2. Sum of 20964 diffraction patterns collected during 220 nm PS-particle injection; experimental data is provided in the red boxes (a, d) and compared to the fitted model. The left figure shows a section of the left half (a) and the right half (d) of the upper detector. The corresponding modeled sections (b, c) are flipped at the horizontal axis to allow for a detailed comparison. (e) Radial plot comparing the angularly integrated experimental and simulated data. Black stripes in the experimental data (a, d) are masked pixels and the exact same pixels were masked in the model in order to ensure comparability.

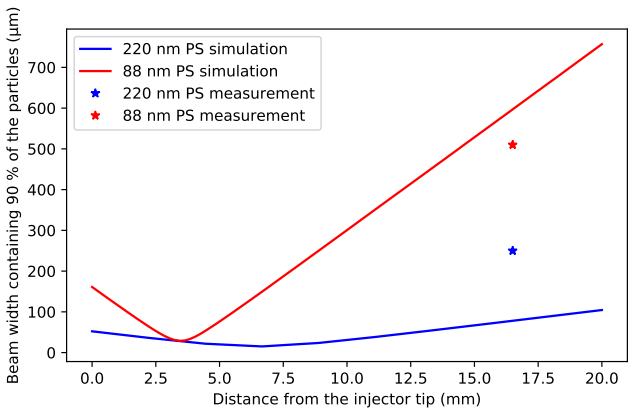


FIG. 3. Simulated beam width containing 90 % of the particles for different distances to the injector tip for 220 nm and 88 nm polystyrene spheres. The measured beam widths are marked as single points with a star, see text and Fig. 4 for details.

of the particles at different distances to the injector tip. The particle beam for 220 nm is overall narrower and has its focus at ∼7 mm downstream the injector tip. The focus of the 88 nm beam is roughly a factor two closer to the tip at ∼3 mm and the beam has a much higher convergence before and divergence after its focus. For comparison, the experimentally observed beam widths for both sizes are depicted by stars in Fig. 3. The measurement reflects the tendency of the 88 nm beam to be broader at this position, but the simulations are clearly underestimating the observed 220 nm beam width.

Measured and simulated beam profiles of the two particle sizes at this position, $z = 16.5$ mm, are shown in Fig. 4. The beam profiles for the 220 nm PS particles

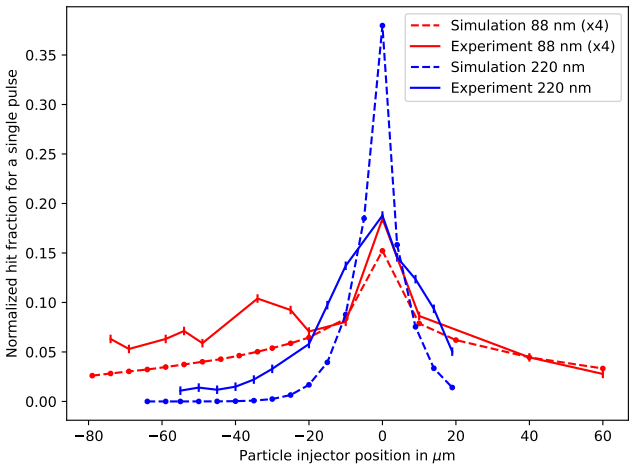


FIG. 4. Measured and simulated hit fraction for a single x-ray pulse dependent on the transverse injector position relative to the x-ray focus. The data for 88 nm PS particle was scaled by a factor of 4 for better visibility.

(blue) show a clear peak and a fast fall off, graphically comparable to a Lorentz function, but with the experimental beam being broader than the simulated profile. The beam profiles for the 88 nm PS spheres (red) also show a peak in the center, but a much slower fall off and even still significant population at the edges of the measurement window. This behavior is present for both, the measured and the simulated profile.

As previously mentioned, for this experimental campaign the ALS was not optimized for a specific size, but to transmit particles in a broad size range from 40 to 300 nm well. Also the geometry and injection conditions were kept constant. Hence, it is expected that the focusing behavior of the ALS for 220 nm and 88 nm differs substantially. Especially for particles below 100 nm optimization of the injector conditions is usually quite challenging [13, 20] and without specific optimization a broader beam profile compared to beams of larger particles is expected. The 88 nm particles are not only smaller but also lighter, hence at the same flow conditions they get accelerated to higher radial velocities and indeed this is what we observe in Fig. 3. The slow fall off in the beam profile is actually a behavior that was previously observed and explained by too high radial acceleration of the particles at individual ADLs within the injector [13]. This also explains why we do not see this effect for 220 nm particles, since their higher mass and inertia leads to less extreme focusing mitigating these effects.

While underestimating the beam width for 220 nm particles, these simulations clearly reflect the major aspects of the measured data. With only one measurement point it is challenging to provide a detailed explanation for the deviation between simulation and experiment in the case of 220 nm PS, but one possible reason is that the 220 nm particle beam is almost collimated. Hence, the position of the focus is a lot more sensitive to experimental imprecisions not reflected in the simulations. For instance, a systematic error on the measured pressure before the ALS could significantly change how hard the 220 nm beam is focused, while the 88 nm beam is already at its extreme.

In any case, the results provided here demonstrate that the described new flexible ALS injector setup with novel capabilities for fast exchange and geometry adjustments works very well for the injection of nanoparticles in SPI experiments.

## IV. CONCLUSION

SPI experiments have the potential to unravel the time-dependent three-dimensional structure of complex biomolecules such as proteins or protein complexes, but they have very demanding requirements for the sample injection. In order to be able to provide the necessary densities for efficient SPI experiments the injector needs to be optimized for every individual sample. Here, we established a new aerodynamic lens injector, tailor made for such experiments, that allows for quick exchange of

the geometry and allows optimization of the injection system beyond the adoption of carrier gas pressures.

Besides the successful first operation under SPI conditions at an FEL, the resulting particle beams could be well predicted using our simulation framework [13, 19]. The simulations showed that the focus of the particle beams for both samples was closer to the injector tip than the mechanical limitations of the setup allowed. This shows how crucial it is not only to characterize the injection system in advance utilizing simulations, but also to be able to adopt the geometry of the injector for optimized experimental conditions for each sample, especially when moving to smaller samples where the amount of scattering signal and also the transmission of the sample decreases. Our new flexible ALS system introduced here will simplify and speed up this optimization process. Generating high-density particle beams of small nanoparticles and bio-macromolecules with reduced background gas will provide useful for furthering the field of single-particle imaging and will also open up the field of time-resolved imaging of nanoparticle dynamics in pump-probe type experiments at XFELs [10].

The analysis of the diffraction patterns of 220 nm PS spheres also yielded the *a priori* unknown complex refractive index of this material of $m = 0.976 - 0.001i$ at $\lambda = 4.5$ nm.

## DECLARATION OF COMPETING INTERESTS

The authors declare that they have no known competing financial interests or personal relationships that could have appeared to influence the work reported in this paper.

## ACKNOWLEDGMENTS

We acknowledge Deutsches Elektronen-Synchrotron DESY, a member of the Helmholtz Association (HGF) for financial support as well as for the provision of experimental facilities and the Maxwell computational resources. Beamtime was allocated for proposal F-20170537. We acknowledge the Max Planck Society for funding the development and the initial operation of the CAMP end-station within the Max Planck Advanced Study Group at CFEL and for providing this equipment for CAMP@FLASH. The installation of CAMP@FLASH was partially funded by the BMBF (grants 05K10KT2, 05K13KT2, 05K16KT3 and 05K10KTB from FSP-302). This work was supported by the European Research Council under the European Union's Seventh Framework Program (FP7/2007-2013) through the Consolidator Grant COMOTION (614507), the Helmholtz Impuls und Vernetzungsfond, and the federal clusters of excellence "Center for Ultrafast Imaging" (CUI, EXC 1074, ID 194651731)) and "Advanced Imaging of Matter" (AIM, EXC 2056, ID 390715994) of the Deutsche Forschungsgemeinschaft (DFG).

## DATA AVAILABILITY

The data that support the findings of this study, including CAD models of the injector setup, are available from the corresponding author upon reasonable request.

[1] M. J. Bogan, W. H. Benner, S. Boutet, U. Rohner, M. Frank, A. Barty, M. M. Seibert, F. Maia, S. Marchesini, S. Bajt, B. Woods, V. Riot, S. P. Hau-Riege, M. Svenda, E. Marklund, E. Spiller, J. Hajdu, and H. N. Chapman, Single particle x-ray diffractive imaging, Nano Lett. **8**, 310 (2008).

[2] M. M. Seibert, T. Ekeberg, F. R. N. C. Maia, M. Svenda, J. Andreasson, O. Jönsson, D. Odić, B. Iwan, A. Rocker, D. Westphal, M. Hantke, D. P. Deponte, A. Barty, J. Schulz, L. Gumprecht, N. Coppola, A. Aquila, M. Liang, T. A. White, A. Martin, C. Caleman, S. Stern, C. Abergel, V. Seltzer, J.-M. Claverie, C. Bostedt, J. D. Bozek, S. Boutet, A. A. Miahnahri, M. Messerschmidt, J. Krzywinski, G. Williams, K. O. Hodgson, M. J. Bogan, C. Y. Hampton, R. G. Sierra, D. Starodub, I. Andersson, S. Bajt, M. Barthelmess, J. C. H. Spence, P. Fromme, U. Weierstall, R. Kirian, M. Hunter, R. B. Doak, S. Marchesini, S. P. Hau-Riege, M. Frank, R. L. Shoeman, L. Lomb, S. W. Epp, R. Hartmann, D. Rolles, A. Rudenko, C. Schmidt, L. Foucar, N. Kimmel, P. Holl, B. Rudek, B. Erk, A. Hömke, C. Reich, D. Pietschner, G. Weidenspointner, L. Strüder, G. Hauser, H. Gorke, J. Ullrich, I. Schlichting, S. Herrmann, G. Schaller, F. Schopper, H. Soltau, K.-U. Kühnel, R. Andritschke, C.-D. Schröter, F. Krasniqi, M. Bott, S. Schorb, D. Rupp, M. Adolph, T. Gorkhover, H. Hirsemann, G. Potdevin, H. Graafsma, B. Nilsson, H. N. Chapman, and J. Hajdu, Single mimivirus particles intercepted and imaged with an X-ray laser, Nature **470**, 78 (2011).

[3] R. Neutze, R. Wouts, D. van der Spoel, E. Weckert, and J. Hajdu, Potential for biomolecular imaging with femtosecond x-ray pulses, Nature **406**, 752 (2000).

[4] M. J. Bogan, S. Boutet, H. N. Chapman, S. Marchesini, A. Barty, W. H. Benner, U. Rohner, M. Frank, S. P. Hau-Riege, S. Bajt, B. Woods, M. M. Seibert, B. Iwan, N. Timneanu, J. Hajdu, and J. Schulz, Aerosol imaging with a soft x-ray free electron laser, Aerosol Sci. Techn. **44**, i (2010).

[5] T. Ekeberg, M. Svenda, C. Abergel, F. R. N. C. Maia, V. Seltzer, J.-M. Claverie, M. Hantke, O. Jönsson, C. Nettelblad, G. van der Schot, M. Liang, D. P. Deponte, A. Barty, M. M. Seibert, B. Iwan, I. Andersson, N. D. Loh, A. V. Martin, H. Chapman, C. Bostedt, J. D. Bozek, K. R. Ferguson, J. Krzywinski, S. W. Epp, D. Rolles, A. Rudenko, R. Hartmann, N. Kimmel, and J. Hajdu, Three-dimensional reconstruction of the giant mimivirus particle with an x-ray free-electron laser, Phys. Rev. Lett. **114**, 098102 (2015).

[6] K. Ayyer, A. J. Morgan, A. Aquila, H. DeMirci, B. G. Hogue, R. A. Kirian, P. L. Xavier, C. H. Yoon, H. N. Chapman, and A. Barty, Low-signal limit of x-ray single particle diffractive imaging, Opt. Exp. **27**, 37816 (2019).

[7] H. N. Chapman, X-ray imaging beyond the limits, Nature Mater. **8**, 299 (2009).

[8] M. F. Hantke, D. Hasse, M. R. N. C, T. Ekeberg, K. John, M. Svenda, N. D. Loh, A. V. Martin, N. Timneanu, L. S. D, van der SchotGijs, G. H. Carlsson, M. Ingelman, J. Andreasson, D. Westphal, M. Liang, F. Stellato, D. P. DePonte, R. Hartmann, N. Kimmel, R. A. Kirian, M. M. Seibert, K. Mühlig, S. Schorb, K. Ferguson, C. Bostedt, S. Carron, J. D. Bozek, D. Rolles, A. Rudenko, S. Epp, H. N. Chapman, A. Barty, J. Hajdu, and I. Andersson, High-throughput imaging of heterogeneous cell organelles with an x-ray laser, Nat. Photon. **8**, 943 (2014).

[9] K. Ayyer, P. L. Xavier, J. Bielecki, Z. Shen, B. J. Daurer, A. K. Samanta, S. Awel, R. Bean, A. Barty, M. Bergemann, T. Ekeberg, A. D. Estillore, H. Fangohr, K. Giewekemeyer, M. S. Hunter, M. Karnevskiy, R. A. Kirian, H. Kirkwood, Y. Kim, J. Koliyadu, H. Lange, R. Letrun, J. Lübke, T. Michelat, A. J. Morgan, N. Roth, T. Sato, M. Sikorski, F. Schulz, J. C. H. Spence, P. Vagovic, T. Wollweber, L. Worbs, O. Yefanov, Y. Zhuang, F. R. N. C. Maia, D. A. Horke, J. Küpper, N. D. Loh, A. P. Mancuso, and H. N. Chapman, 3D diffractive imaging of nanoparticle ensembles using an x-ray laser, Optica **8**, 15 (2021), arXiv:2007.13597 [physics].

[10] D. Höing, R. Salzwedel, L. Worbs, Y. Zhuang, A. Samanta, J. Lübke, A. D. Estillore, K. Dlugolecki, C. Passow, B. Erk, N. Ekanayake, D. Ramm, J. Correa, C. C. Papadopoulou, A. T. Noor, F. Schulz, M. Selig, A. Knorr, K. Ayyer, J. Küpper, and H. Lange, Time-resolved single-particle x-ray scattering reveals electron-density gradients as coherent plasmonic-nanoparticle-oscillation source, Nano Lett. **23**, 5943–5950 (2023).

[11] D. P. DePonte, U. Weierstall, K. Schmidt, J. Warner, D. Starodub, J. C. H. Spence, and R. B. Doak, Gas dynamic virtual nozzle for generation of microscopic droplet streams, J. Phys. D **41**, 195505 (2008).

[12] S. Awel, R. A. Kirian, M. O. Wiedorn, K. R. Beyerlein, N. Roth, D. A. Horke, D. Oberthür, J. Knoska, V. Mariani, A. Morgan, L. Adriano, A. Tolstikova, P. L. Xavier, O. Yefanov, A. Aquila, A. Barty, S. Roy-Chowdhury, M. S. Hunter, D. James, J. S. Robinson, U. Weierstall, A. V. Rode, S. Bajt, J. Küpper, and H. N. Chapman, Femtosecond X-ray diffraction from an aerosolized beam of protein nanocrystals, J. Appl. Cryst. **51**, 133 (2018), arXiv:1702.04014.

[13] N. Roth, S. Awel, D. A. Horke, and J. Küpper, Optimizing aerodynamic lenses for single-particle imaging, J. Aerosol. Sci. **124**, 17 (2018), arXiv:1712.01795 [physics].

[14] S. Awel, R. A. Kirian, N. Eckerskorn, M. Wiedorn, D. A. Horke, A. V. Rode, J. Küpper, and H. N. Chapman, Visualizing aerosol-particle injection for diffractive-imaging experiments, Opt. Exp. **24**, 6507 (2016), arXiv:1512.06231 [physics].

[15] B. Erk, J. P. Müller, C. Bomme, R. Boll, G. Brenner, H. N. Chapman, J. Correa, S. Düsterer, S. Dziarzhytski, S. Eisebitt, H. Graafsma, S. Grunewald, L. Gumprecht, R. Hartmann, G. Hauser, B. Keitel, C. von Korff Schmising, M. Kuhlmann, B. Manschwetus, L. Mercadier, E. Müller, C. Passow, E. Plönjes, D. Ramm, D. Rompotis, A. Rudenko, D. Rupp, M. Sauppe, F. Siewert, D. Schlosser, L. Strüder, A. Swiderski, S. Techert, K. Tiedtke, T. Tilp, R. Treusch, I. Schlichting, J. Ullrich, R. Moshammer, T. Möller, and D. Rolles, CAMP@FLASH: an end-station for imaging, electron- and ion-spectroscopy, and pump–probe experiments at the FLASH free-electron laser, J. Synchrotron Rad. **25**, 1529 (2018).

[16] J. Feldhaus, FLASH – the first soft x-ray free electron laser (FEL) user facility, J. Phys. B **43**, 194002 (2010).

[17] M. O. Wiedorn, S. Awel, A. J. Morgan, M. Barthelmess, R. Bean, K. R. Beyerlein, L. M. G. Chavas, N. Eckerskorn, H. Fleckenstein, M. Heymann, D. A. Horke, J. Knoška, V. Mariani, D. Oberthür, N. Roth, O. Yefanov, A. Barty, S. Bajt, J. Küpper, A. V. Rode, R. A. Kirian, and H. N. Chapman, Post-sample aperture for low background diffraction experiments at x-ray free-electron lasers, J. Synchrotron Rad. **24**, 1296 (2017).

[18] L. Strüder, S. Epp, D. Rolles, R. Hartmann, P. Holl, G. Lutz, H. Soltau, R. Eckart, C. Reich, K. Heinzinger, C. Thamm, A. Rudenko, F. Krasniqi, K. Kühnel, C. Bauer, C.-D. Schroeter, R. Moshammer, S. Techert, D. Miessner, M. Porro, O. Haelker, N. Meidinger, N. Kimmel, R. Andritschke, F. Schopper, G. Weidenspointner, A. Ziegler, D. Pietschner, S. Herrmann, U. Pietsch, A. Walenta, W. Leitenberger, C. Bostedt, T. Moeller, D. Rupp, M. Adolph, H. Graafsma, H. Hirsemann, K. Gaertner, R. Richter, L. Foucar, R. L. Shoeman, I. Schlichting, and J. Ullrich, Large-format, high-speed, X-ray pnCCDs combined with electron and ion imaging spectrometers in a multipurpose chamber for experiments at 4th generation light sources, Nucl. Instrum. Methods Phys. Res. A **614**, 483 (2010).

[19] S. Welker, M. Amin, and J. Küpper, CMInject: Python framework for the numerical simulation of nanoparticle injection pipelines, Comp. Phys. Comm. **270**, 108138 (2022).

[20] L. Worbs, N. Roth, J. Lübke, A. D. Estillore, P. L. Xavier, A. K. Samanta, and J. Küpper, Optimizing the geometry of aerodynamic lens injectors for single-particle coherent diffractive imaging of gold nanoparticles, J. Appl. Cryst. **54**, 1730 (2021), arXiv:2105.15084v1 [physics].

[21] COMSOL Multiphysics v. 5.3. `http://www.comsol.com`. COMSOL AB, Stockholm, Sweden.

[22] S. Prahl, miepython, Website, URL: `https://github.com/scottprahl/miepython` (2019), accessed on 2019-10-05.

[23] A. Thompson, I. Lindau, D. Attwood, Y. Liu, E. Gullikson, P. Pianetta, M. Howells, A. Robinson, K.-J. Kim, J. Scofield, J. Kirz, J. Underwood, J. Kortright, G. Williams, and H. Winick, *X-Ray Data Booklet* (Center for X-Ray Optics and Advanced Light Source, Lawrence Berkeley National Laboratory, Berkeley, CA, 2009).